EFFECT OF TiO_2 ADDITION ON ELASTIC MODULI, OPTICAL BANDGAP, AND ELECTRICAL CONDUCTIVITY OF $xTiO_2$-(0.30-x)Bi_2O_3-0.10ZnO-0.60TeO_2 GLASSY SYSTEMS WITH IMPROVED THERMAL STABILITY

Reference NO. IJME 1375, DOI: 10.5750/ijme.v1i1.1375

Dipankar Biswas*, Department of Electronics and Communication Engineering, Institute of Engineering and Technology, GLA University, Mathura, UP 281406, India, **Arpan Mandal,** Department of Mechanical Engineering, Jadavpur University, Kolkata 700032, West Bengal, India, **Souvik Brahma Hota**, Department of Mechanical Engineering, Techno India University, Kolkata 700091, West Bengal, India, **Ashok Kumar**, Chitkara Centre for Research and Development, Chitkara University, Himachal Pradesh, India, **Gopal Krishan Gard**, Centre of Research Impact and Outreach, Chitkara University, Rajpura-140401, Punjab, India, **Rittwick Mondal,** Department of Science, Chowhatta High School, Birbhum 731201, West Bengal, India and **Nipu Modak,** Department of Mechanical Engineering, Jadavpur University, Kolkata 700032, West Bengal, India

*Corresponding author. Dipankar Biswas (Email): biswas.dipankar3579@gmail.com

KEY DATES: Submission date: 25.12.2023 / Final acceptance date: 20.02.2024 / Published date: 12.07.2024

SUMMARY

Glassy systems with the chemical composition $xTiO_2$-(0.30-x)Bi_2O_3-0.10ZnO-0.60TeO_2 (x = 0.05,0.10,0.15,0.20) have been synthesized using the melt quench approach. Numerous physical, electrical, optical, and other features of elastic moduli have been evaluated as titanium oxide concentration rises. The amorphous properties of the materials under inspection are displayed in the XRD pattern. As the concentration of arsenic rises, the glasses' density falls from 4.18 to 3.96 g/cm^3, while their molar volume rises from 48.21 to 53.06 cm^3mol^{-1}. The elastic properties of the synthesized glasses, such as the shear (S) and longitudinal (L) stresses, bulk modulus (K), Young's modulus (Y), and Poisson's ratio (Pr), have all been measured using the measured values of the ultrasonic velocities. The increase in elastic moduli values showed that the materials' elastic qualities have been improved. The results are explained in terms of a significant structural alteration caused by molecular rearrangement, which controls the physical properties of the glass. The addition of titanium oxide is shown to cause a decrease in Urbach energies from 0.96 to 0.67 eV, which results in an increase in the optical band gap energies from 2.96 to 3.33 eV. DSC thermogram measurements reveal mechanically enhanced and thermally stable materials with potential for use in semiconducting devices.

KEYWORDS

Young's modulus, Optical band gap energy, DC conductivity, DSC thermogram

1. INTRODUCTION

Tellurite-based glasses often surpass phosphates, germinates, and silicates in physical and optical properties (Mandal et al., 2023). Tellurite glass features a high refractive index, making it attractive for various optoelectronic applications (El-Mallawany et al., 2021). Researchers are increasingly exploring TeO2-based glasses for applications in high-performance lasers, broadband amplifiers, optical fibers, light-emitting materials, telecommunications, and other advanced technologies. (Biswas and Jana, 2023). Adding modifying oxides, which act as network modifiers, is common practice to stabilize tellurite glass due to TeO2's poor glass-forming ability (Mondal et al., 2020). ZnO reduces the crystallization rate and lowers the melting point, enhancing glass-forming potential (Mondal et al., 2020). It is anticipated that Oxide modifiers can break certain TeO4 units in tellurite glasses. Te ion coordination numbers concerning oxygen ions shift, causing tellurite's structural units to transform from a trigonal bi-pyramid TeO_4 to a distorted polyhedron TeO_{3+1} and finally a trigonal pyramid (t_p) TeO_3 (Lucacel et al., 2010). Tellurium ion coordination modification produces both bridging and non-bridging oxygen, which interacts with neighboring tellurium atoms to create modifier atoms (Sidek et al., 2009). Because of its functions as a modulator and network former in the glass network, bismuth oxide (Bi_2O_3) stands out among heavy metal oxides when added to tellurite glasses (Shaaban and Yousef, 2020). Bi_2O_3 addition increases the glasses' stability and chemical resistance. By raising density and refractive index, Bi_2O_3 serves as both a glass forming and a glass modifier (Rao et al., 1985). Glasses with heavy metal oxide modifiers like Bi_2O_3 enhance transmission windows and nonlinear optical traits in tellurite glasses, making them promising for photonics, signal processing, and

optoelectronics (Berwal et al., 2017). Researchers have studied Bi_2O_3 incorporated tertiary tellurite-based glass in several investigations. In the interim, additives like Gd_2O_3, Cr_2O_3, CaF_2, Fe_2O_3, TiO_2, etc. are typically added to the base system as property modifiers to generate more sophisticated glassy systems (Hathot et al., 2021, Zhang et al., 2019). TiO_2's addition attracts attention for enhancing glassy systems' electrical, mechanical, spectroscopic properties, and thermal stability, among others (Osipov et al., 2020). Additionally, it has been discovered that TeO_2-based glassy systems have been promising and had applications in laser-operated devices (Narasimha Rao et al., 2012). However, due to the stiffness of the octahedral Te-O polyhedron, TeO_2 is an emerging glass former that is difficult to form glass alone under typical synthesising circumstances (Elkhoshkhany and Syala, 2017).

In previous studies, Murugan et, al have studied temperature assisted electrical properties of TeO_2-Bi_2O_3-ZnO glasses (Murugan et al., 2004), Kabalci et.al have studied the structure, and hardness competence of TeO_2-Bi_2O_3-ZnO glasses (Kabalci et al., 2017), Fong et.al have studied the thermal, and optical properties of Bi_2O_3-TiO_2-Na_2O-ZnO-TeO_2 glasses (Fong et al., 2021) for various optoelectronic applications. Recent research explores nanocomposites for potential in photonics and dielectric applications (Al-Muntaser et al., 2022).

The primary objective of the current work is to gain a deep realization of the role of TiO_2 on the glass network structure, and electrical, mechanical, and optical properties of TiO_2-Bi_2O_3-ZnO-TeO_2 glassy systems in addition to investigating its capability as an electro-optical material in semiconducting photonic device applications, thereby contributing to the advancement of glass nanocomposite technology for various applications.

2. MATERIALS AND METHODS

2.1 SAMPLE PREPARATION

The $xTiO_2$-(0.30-x)Bi_2O_3-0.10ZnO-0.60TeO_2 (x = 0.05, 0.10, 0.15, 0.20) quaternary glass nanocomposites were prepared by finely crushing precise quantities of high-purity raw chemicals, including TeO_2, Bi_2O_3, TiO_2, and ZnO (99.9% as pure), in an agate mortar to achieve a homogeneous powder. The mixtures were heated in alumina crucibles in an electric furnace under atmospheric air conditions until reaching melting points, ranging from 1100-1200 °C. Each stage of the melting process requires careful observation. To enhance melt fluidity, it was kept at the melting temperature in an electric furnace for 30 extra minutes. The melts were swiftly quenched at room temperature using a polished aluminum melt-quencher, yielding glassy flakes 0.3 to 0.5 mm thick. The prepared samples were annealed at 350°C to alleviate internal stress from the quenching process.

2.2 PHYSICAL MEASUREMENT TECHNIQUE

Molecular weight, constituent proportions, and glass structure collectively impact oxide glass density (ρ). The Archimedes equation (Eq. (1)) determined glassy systems' densities using acetone as the immersion liquid (Singh et al., 2021b).

$$\rho = \rho_{acetone}\left(\frac{W_{air}}{W_{air} - W_{acetone}}\right) \quad (1)$$

In Eq. 1, W_{air} and $W_{acetone}$ are the measured weights of the glass sample in air and acetone, respectively, while ρacetone is acetone's density. The density (ρ) of each glass sample was determined from three pieces, and an average was taken to reduce inaccuracies. Weights were measured using a digital balance with a precision of 10^{-4} g.

The molar volume (V_M) of the glass system, a crucial physical parameter, can be calculated using Eq. (2), which incorporates the molecular weight (M) and the estimated density (ρ) of the glass system (Singh et al., 2021b).

$$V_M = \sum \frac{x_i M_i}{\rho} \quad (2)$$

In Eq. (2), x_i and M_i represent the molar fraction and molecular weight of the i^{th} glass composition, respectively.

2.3 CHARACTERIZATION TECHNIQUE

A study employing X-ray diffraction (XRD) was conducted on each glass sample to verify its amorphous nature. Rigaku TTRAX-III XRD diffractometer was used, with CuKa radiation (λ = 1.541 Å), scanning at 4°/min with a step size of 0.02 over 15 to 80 degrees.

2.4 MEASUREMENT OF MECHANICAL PARAMETERS

The study utilized an ultrasonic flow detector (USN 60) with the pulse-echo-overlap technique at room temperature. Longitudinal and shear transducers with a frequency of 5MHz were employed. Ultrasonic velocity (v) was determined by selecting the first two echo signals (A1, A2) and their corresponding times (t1, t2) in the sample (Saddeek et al., 2010),

$$\upsilon = \frac{2X}{t_2 - t_1} \quad (3)$$

Here, with pulse time (t) in seconds and sample thickness (X), shear (S) and longitudinal (L) strains were calculated using measured values of $\mathbf{v}_L$, $\mathbf{v}_T$ and ρ following specific relations. $L = \rho v_L^2$, and $S = \rho v_T^2$ (Saddeek et al., 2019). The Poisson ratio (Pr), Young (Y), and Bulk (K) moduli

were calculated by calculating the S and L values in the manner described below (Saddeek et al., 2019) [35]:

$$K = L - 1.33S \tag{4}$$

$$P_r = (L - 2S)(2L - 2S)^{-1} \tag{5}$$

$$Y = 2S(1 + P_r) \tag{6}$$

2.5 DIRECT CURRENT MEASUREMENTS

High-temperature conductive silver paste was applied to bulk materials in order to prepare them as electrodes for electrical research. A two-point probe method was used to test the DC electrical conductivity. Using a digital multimeter, sample resistances quenched at different temperatures were determined. A calibrated thermocouple that was positioned close to the sample in the furnace was used to track the temperature. With a ± 5% error tolerance, the temperature controller unit and thermocouple were utilized to accurately calculate the glass's operating temperature. Between 423 K and 623 K, the temperature dependency of DC electrical conductivity was carefully assessed.

2.6 OPTICAL MEASUREMENTS

Optical absorption spectra (190–700 nm) were acquired at room temperature using a Shimadzu NIR 3600 UV–Vis spectrophotometer in reflectance mode. Colloidal suspensions for absorption were prepared by homogenizing fine powder glass samples in ethyl alcohol with an ultrasonic sonicator (Takashi SK-500F). If we assume the indirect transition, we may express the absorption coefficient (α) as follows (Biswas et al., 2023):

$$(\alpha h\upsilon)^{1/2} = B(h\upsilon - E_{opt}) \tag{7}$$

In this case, the optical band gap energy is represented by E_{opt}, the photon energy is represented by hυ, and the constant parameter is B. Tauc's plot is the plot of $(\alpha h\upsilon)^{1/2}$ against hυ (Biswas et al., 2023).

Here, $\alpha(\upsilon) = 2.303 \dfrac{Absorbance}{samplethickness}$ (8)

3. RESULT AND DISCUSSION

3.1 X-RAY DIFFRACTION

As depicted in Figure 1, the XRD patterns of the $xTiO_2$-$(0.30\text{-}x)Bi_2O_3$-$0.10ZnO$-$0.60TeO_2$ samples illustrates no significant peaks aside from the broad peak due to glass structure. The materials lack crystallinity, displaying

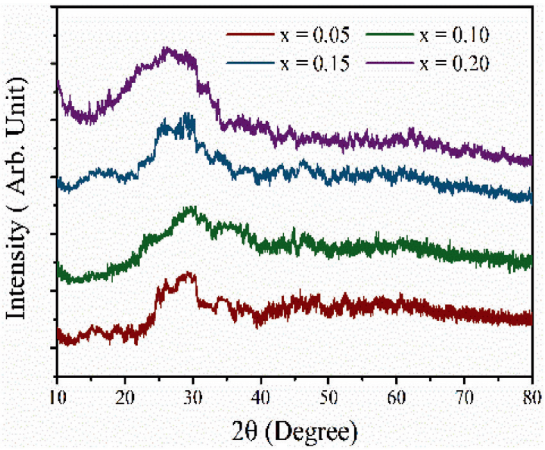

Figure 1. XRD patterns glassy systems

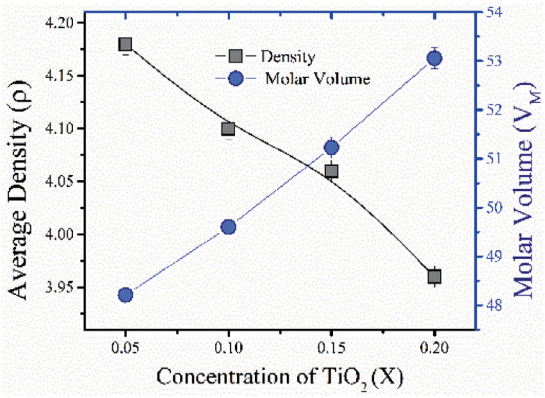

Figure 2. Variation of density and molar volume with TiO_2 content (x)

a broad hump (20–40 degrees) without sharp peaks, suggesting a non-crystalline, amorphous, or short-range ordered structure (Mondal et al., 2023).

3.2 STUDY OF DENSITY AND MOLAR VOLUME

Density is a key factor in understanding structural changes and compactness in the glass network, influencing thermal, elastic, and optical properties. Computed density (ρ) values, obtained using Eq. 1, are plotted against TiO_2 concentration (x) in Figure 2. Molar volume, vital for analyzing structural characteristics, is correlated with density.

Eq. 2 can be used to find the glassy system's molar volume. As shown in some earlier research, it is evident from Figure 2 that there is an inverse relationship between density and molar volume. All the obtained values of densities and molar volumes

Table 1. Obtained physical, and optical parameters of studied glass samples

x	Density (ρ) g/cm³	Molar volume (V_M) cm³	Bandgap energy (E_{opt}) eV	Urbach energy (ΔE) eV
0.05	4.18	48.21	2.96	0.96
0.10	4.10	49.60	3.05	0.87
0.15	4.06	51.23	3.27	0.72
0.20	3.96	53.06	3.33	0.67

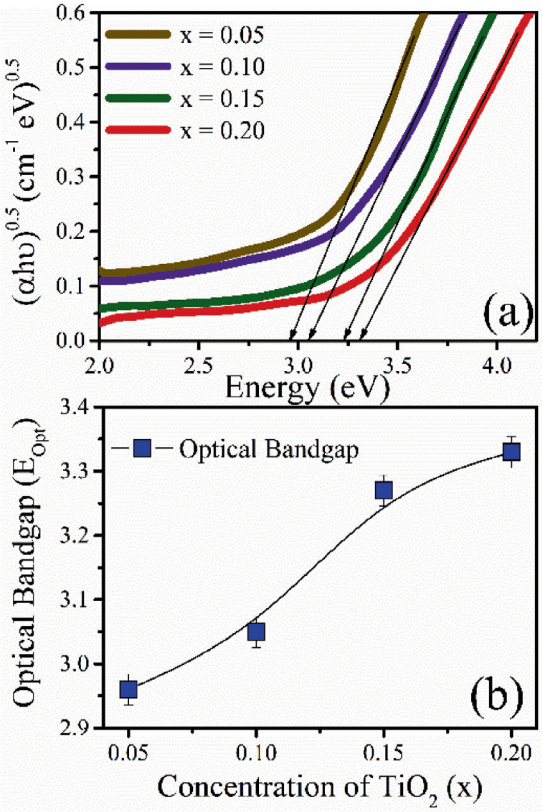

Figure 3. (a) Tauc's plot of studied samples, (b) variation of E_g Titanium oxide content (x)

are tabulated in Table 1. The decrease in density (ρ) is attributed to the replacement of higher-density Bismuth oxide with lower-density Titanium oxide atoms (Elkhoshkhany et al., 2016). The increase in molar volume (VM) results from lattice rearrangement due to TiO_2 replacing Bi_2O_3, expanding the structure and increasing the ring size (Elkhoshkhany et al., 2016).

3.3 STUDY OF OPTICAL BAND GAP ENERGY AND URBACH ENERGY

Disordered materials show an absorption edge attributed to indirect transitions across an optical gap, as explained by the electronic structure theory of amorphous materials.

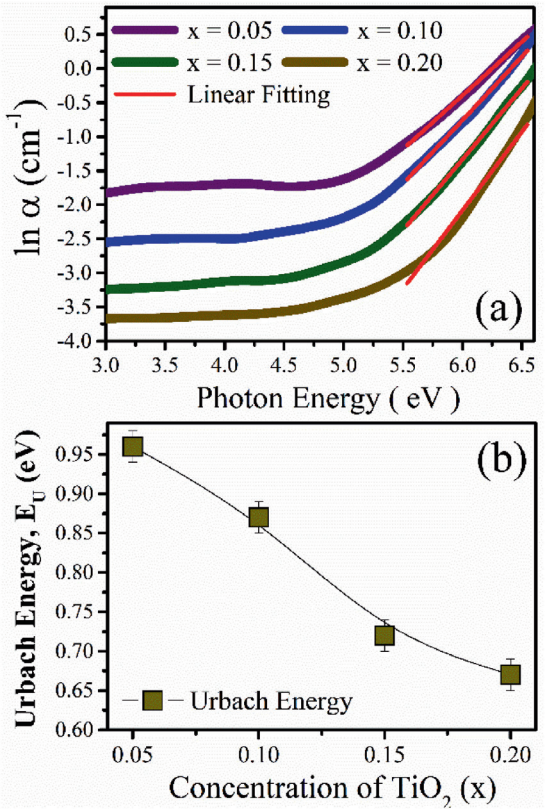

Figure 4. (a) variation of ln (α) against hν (b) variation of E_U with Titanium oxide content(x)

By taking a graph of the variation of $(\alpha h\upsilon)^{1/2}$ vs hυ and projecting the linear region to the x-axis when α = 0 of the curves, one can use a Tauc approach to get optical energy band gap values (Figure 3(a)) (Singh et al., 2021a).

Table 1 and Figure 3(b) summarize E_g values for glasses with varying titanium oxide percentages. As titanium oxide content increases, replacing bismuth oxide, the band gap energy grows from 2.96 to 3.33 eV. This rise may be attributed to the higher band gap energy of titanium oxide compared to bismuth oxide. Additionally, a decrease in Urbach energy levels could contribute to the increasing E_{opt} value.

To assess disorder in materials, Urbach energy (E_U) is crucial. The band tail width (E_U) is associated with electron transitions between localized states, exhibiting an exponential pattern due to random potential variations in the material's energy released into the bandgap. Regardless of substance composition, the experimental tail stems from localized states within the restricted band-gap region.

The Urbach energy (E_U) can be obtained by plotting ln(α) against photon energy (Figure 4(a)) and using the empirical relation (Urbach, 1953):

$$\alpha(\upsilon) = \alpha_0 exp\left(\frac{h\upsilon}{\Delta E}\right) \quad (9)$$

The resulting values of E_U are shown in Figure 4(b). It's interesting to note that as titanium oxide is incorporated into the host matrix in greater numbers, Urbach energy drops, which raises the E_{opt} of the materials under study (Table 1). Previous studies have indicated an inverse relationship between the E_g and E_U (El Ghandoor et al., 2012).

3.4 STUDY OF ULTRASONIC WAVE VELOCITIES AND ELASTIC MODULI

Table 2 lists the longitudinal velocity (v_L) and shear velocity (v_T) data that were acquired and recorded at room temperature. Figure 5 shows how the Titanium content (x) varies with longitudinal and shear velocities.

With increased Titanium oxide in the glassy matrix, both $\mathbf{v}_L$, $\mathbf{v}_T$ rise from 3132 m/s to 3274 m/s and from 1796 m/s to 1878 m/s, respectively. This increase in ultrasonic velocities is attributed to structural changes, molar volume increase, and impedance decrease in the studied glasses. Computed longitudinal modulus (L) and shear modulus (S) rise from 41.00 to 42.66 Gpa and 13.48 to 14.03 Gpa, respectively, as shown in Table 2. Bulk modulus (K), Young's modulus (Y), and Poisson ratio (Pr) values also increase with the addition of Titanium oxide. The elasticity bulk modulus is a crucial mechanical measure for assessing a substance's compression under external pressure. The elastic moduli are extremely significant parameter for a material to inspect to examine the functionalization of that sample (Yadav et al., 2019). The observed increasing trend of Pr (from 0.252-0.254) Gpa signifies good mechanical strength of the studied glasses. It has been demonstrated in the literature that even trace amounts of Titanium oxide can change average connectivity, which in turn can modify crosslink density and, in turn, elastic moduli ,as found in previous study [38].

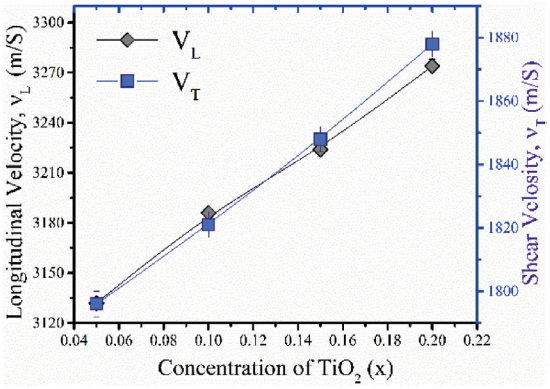

Figure 5. Variation of longitudinal velocity ($\mathbf{v}_L$), and shear velocity ($\mathbf{v}_T$) of studied glasses with Titanium oxide content (x)

Table 2. The mechanical parameters of the studied glasses

x	v_L m/s	v_T m/s	S Gpa	L Gpa	K Gpa	P_r Gpa	Y Gpa
2	3132	1796	13.48	41.00	23.08	0.257	33.75
4	3186	1821	13.59	41.61	23.54	0.256	34.15
6	3224	1848	13.86	42.20	23.77	0.254	34.78
8	3274	1878	14.03	42.66	24.01	0.253	35.18

3.5 DC CONDUCTIVITY

The figure reveals two distinct temperature-dependent conductivities (σ_{dc}) in glassy systems, emphasizing varied conductive behaviors. The non-linear σ_{dc} behavior, increasing with temperature across all systems, strongly supports their inherent semiconducting nature. The amorphous glassy structure introduces extended or localized states within the mobility gap, influencing intricate electronic properties. These states play a crucial role in dictating electrical conductivity, particularly at higher temperatures, where band conduction relies on charge carriers moving across these states. The semiconducting behavior is further confirmed by the Arrhenius equation characterizing the σ_{dc} (Mandal et al., 2023).

$$\sigma_{dc} = \sigma_{High} \exp\left(-\frac{E_{High}}{K_B T}\right) + \sigma_{Low} \exp\left(-\frac{E_{Low}}{K_B T}\right) \quad (10)$$

Conversely, at lower temperatures, the conduction process is dominated by the presence of small polarons or electrons engaging in hopping behaviour (Biswas et al., 2019a). Charge carriers move through different states in the material, including localized, extended, or defect states. Tunnelling between nearby sites also aids conduction at lower temperatures. The intricate interplay between charge carriers and varied conduction mechanisms at different temperature ranges underscores the complexity of semiconducting behavior in glassy systems. The diverse mechanisms in different temperature regimes offer a comprehensive understanding of conductivity phenomena in these materials.

Figure 6 shows σ_{dc} spectra plotted against the reciprocal of temperature, confirming two distinct forms of temperature-dependent σ_{dc}. The non-linear behavior in dc conductivity (σ_{dc}) and the simultaneous increase in σ_{dc} with rising temperature across all glassy systems affirm their inherent semiconducting characteristics. This suggests semiconductor-like properties in electrical conductivity, influenced by temperature changes akin to semiconductors. Eq. (10)'s first section defines the high-temperature zone (σ_{High}), a result of band conduction with extended states within the mobility gap in amorphous glasses. The low-temperature zone (σ_{Low}) characterizes the conduction process arising from tunneling between nearby unoccupied sites or hopping of tiny polarons or electrons through localized or defect states at lower temperatures.

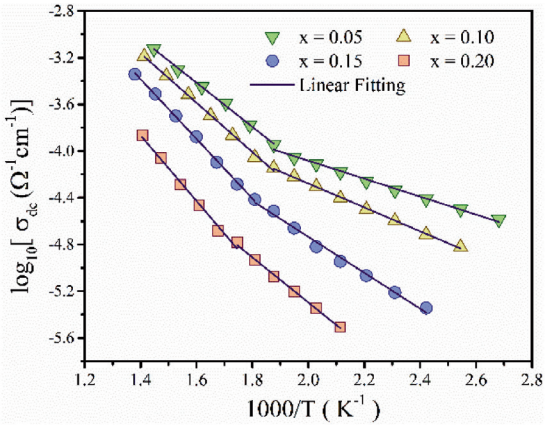

Figure 6. DC Conductivity spectra with reciprocal of temperature

The composition determines pre-exponential factors σ_{High} and σ_{Low}.

At low temperatures within the mobility gap or optical bandgap, conduction involves the hopping of small polarons or charge carriers between localized states, adhering to Mott's variable range hopping (VRH) model (Elliott, 1994).

$$\sigma_{dc} = B\exp\left[-\left(\frac{T_0}{T}\right)^{1/4}\right] \tag{11}$$

and,

$$T_0 = \frac{16\alpha^3}{K_B N(E_{FM})} \tag{12}$$

Mott's VRH model is applicable when localized states exist at the Fermi energy level, and state densities are finite. The Mott's VRH conductivity Eqn. (11-12) is represented, where $N(E_{FM})$ signifies the density of states at the Fermi level, T_0 represents the characteristic temperature, and α^{-1} corresponds to the localization length of the tiny polaron wave function (Biswas et al., 2019b). Figure 7 illustrates the plot of σ_{dc} versus $T^{-0.25}$, showing agreement between experimental values and Eq. (11). The density of states at the Fermi level ($N(E_{FM})$) is evaluated using Eq. (12) with a slope from the linear-fit data in Figure and assuming a value of α^{-1} = 10 Å for localized states.

To predict temperature-dependent parameters associated with small polaron hopping, such as hopping distance (R_{hop}) and average hopping energy (W_{hop}), Eqs. (13) and (14) are utilized (Mandal et al., 2023).

$$R_{hop} = \left(\frac{9}{8\pi N(E_{FM})\alpha K_B T}\right)^{1/4} \tag{13}$$

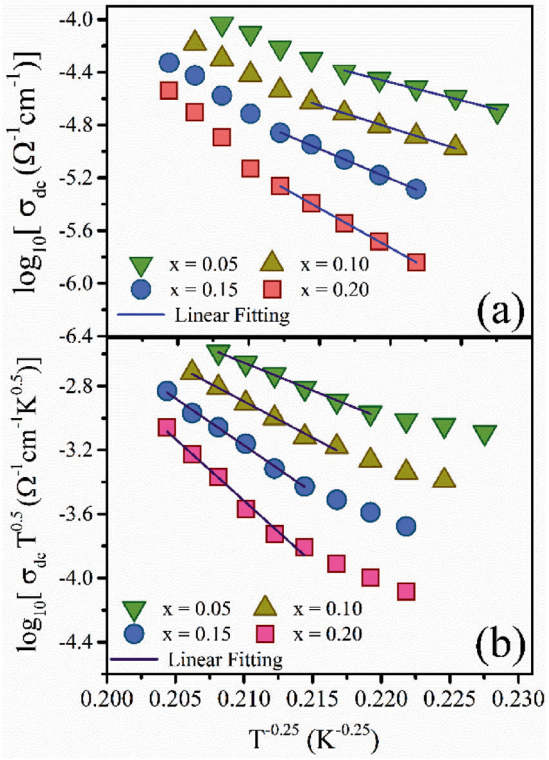

Figure 7. (a) Mott's and (b) Greave's model representation

and,

$$W_{hop} = \frac{3}{4\pi\left(R_{hop}\right)^3 N\left(E_{FM}\right)} \tag{14}$$

The values of R_{hop} and W_{hop} at a fixed temperature (T = 413 K) are detailed in Table 3. It is observed that $R_{hop}\alpha \geq 1$ and $W_{hop} > K_BT$ and $W_{hop} > K_BT$, prerequisites for the validity of Mott's VRH model, are consistently met across all glassy systems. The results in the Table 3 show that as DC conductivity increases, R_{hop} and W_{hop} values decrease with increasing TiO_2 concentration (x), indicating accelerated conduction due to reduced hopping time and energy requirements between nearby sites.

However, Mott's VRH model is not effectively describing the temperature dependence of σ_{dc} spectra higher than half of the Debye temperature ($\theta_{D/2}$). To account for DC conduction at high temperatures ($> \theta_{D/2}$), Greaves proposed an additional equation (Biswas et al., 2023).

$$\sigma_{dc}T^{1/2} = A^{/}\exp\left[-\left(\frac{T_0^{/}}{T}\right)^{1/4}\right] \tag{15}$$

and,

$$T_0^{/} = \frac{19.4\alpha^3}{K_B N\left(E_{FG}\right)} \tag{16}$$

Table 3. Several electrical parameters

Parameters	TiO_2 Content			
	0.05	**0.10**	**0.15**	**0.20**
E_{Low} (eV)	0.42	0.51	0.66	0.79
E_{High} (eV)	1.12	1.24	1.41	1.52
$N(E_{FM})(\times 10^{27}\, eV^{-1}cm^{-3})$	6.11	5.48	5.03	4.12
$N(E_{FG})$ $(\times 10^{27}\, eV^{-1}cm^{-3})$	0.67	0.98	1.12	1.32
R_{Hop} (at 413K) (nm)	3.33	3.65	4.12	4.72
W_{Hop}(at 473K) (meV)	0.61	0.76	0.82	0.98

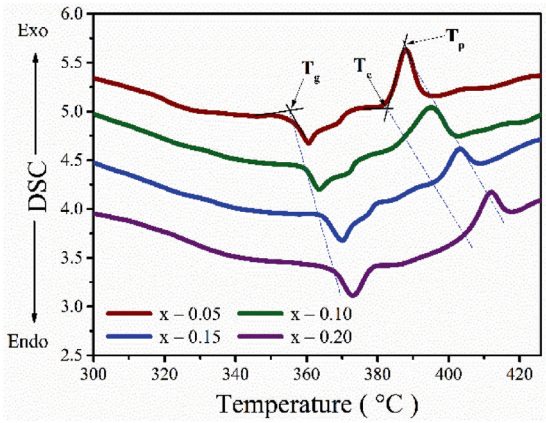

Figure 8. DSC Plot of studied glasses

The Greaves's variable range hopping (VRH) model, represented by equations (15) and (16), is employed to fit σ_{dc} spectra at elevated temperatures. The density of states (DOS) at the Fermi level ($N(E_{FG})$) is determined using Greaves's VRH model by applying Eq. (15) to the slope of the linear-fit data in the high-temperature region, as depicted by the solid lines in Figure 7(b). The values of $N(E_{FM})$ and $N(E_{FG})$ show an decreasing trend with the rising content of TiO_2 (x), as observed in Table 3. This decreasing behavior in $N(E_{FM})$ and $N(E_{FG})$ provides insight into the declining σ_{dc} across all glass systems.

3.6 THERMAL STUDY:

Figure 8 shows DSC curves for the studied glasses, confirming homogeneity with one T_g per composition. Exothermic peaks indicate amorphous-crystalline transitions. Table 4 lists measured thermal parameters, revealing a rise in glass transition temperature with increasing Titanium oxide concentration (x).

These curves can be distinguished by their glass transition temperature (T_g), crystallization temperature (T_c), and peak crystallization temperature (T_p). The graph exhibits an endothermic step at the glass transition temperature, with an exothermic second peak resulting from phase change.

Table 4. Obtained values of thermal parameters

x	T_g (°C)	T_C (°C)	T_P (°C)	$(\Delta T=T_c-T_g)$ (°C)
0.05	356	380	388	24
0.10	361	387	395	26
0.15	367	396	407	29
0.20	371	403	413	32

The crystallization temperature, Tc, increases with rising Titanium oxide concentration (x), along with T_g and T_p values. The samples demonstrate thermal stability across a wide temperature range, suggesting suitability for high-temperature applications. The higher Titanium content enhances stability against crystallization, evidenced by an increase in (Tc-Tg). Therefore, adding TiO_2 to the glassy matrix increases thermal stability, likely due to higher cross-link density and stretching force constants.

4. CONCLUSIONS

In the current experiment, Glass compositions with the formula $xTiO_2$-(0.30-x)Bi_2O_3-0.10ZnO-0.60TeO_2 were synthesized, confirming amorphous nature via XRD. Increasing titanium oxide led to higher molar volume (48.21-53.06cc) and lower density (4.18-3.96g/cc). Density and ultrasonic velocities determined longitudinal and shear strains, resulting in Poisson's ratio and elastic moduli. Elastic moduli increased with more titanium oxide, indicating improved elastic properties. Optical absorption spectrum determined bandgap energy, showing structural changes with TiO_2 concentration. Semiconducting behaviour was observed through temperature-dependent DC conductivity. Mott's VRH model explained low-temperature conduction, while Greaves's VRH model addressed limitations at higher temperatures. Thermal parameters from DSC curve increased with TiO_2 addition, providing insights into complex conductivity mechanisms for potential applications.

5. REFERENCES

1. AL-MUNTASER, A. A., PASHAMEAH, R. A., SHARMA, K., ALZAHRANI, E., FAREA, M. O. & MORSI, M. A. 2022. α-MoO3 nanobelts/CMC-PVA nanocomposites: hybrid materials for optoelectronic and dielectric applications. *Journal of Polymer Research,* 29**,** 274.
2. BERWAL, N., DHANKHAR, S., SHARMA, P., KUNDU, R. S., PUNIA, R. & KISHORE, N. 2017. Physical, structural and optical characterization of silicate modified bismuth-borate-tellurite glasses. *Journal of Molecular Structure,* 1127**,** 636-644.
3. BISWAS, D., MONDAL, R., MANDAL, D. & MONDAL, S. 2023. Investigation on Bi-induced changes on linear and non-linear optical

parameters of As45-Se (55-x)-Bix chalcogenide glasses for photonic application. *Journal of Non-Crystalline Solids,* 614**,** 122401.

4. BISWAS, D., NINGTHEMCHA, R. K. N., DAS, A. S. & SINGH, L. S. 2019a. Structural characterization and electrical conductivity analysis of MoO3–SeO2–ZnO semiconducting glass nanocomposites. *Journal of Non-Crystalline Solids,* 515**,** 21-33.
5. BISWAS, D., SINGH, L. S., DAS, A. S. & BHATTACHARYA, S. 2019b. An investigation of S–Se–Te semiconducting glassy alloys: Structural characterization and electrical conductivity. *Journal of Non-Crystalline Solids,* 510**,** 101-111.
6. BISWAS, J. & JANA, S. 2023. Visible luminescence and energy migration mechanism of Sm3+ in phospho-tellurite glasses by co-activating with Tb3+ ions for solid state lighting device applications. *Physica B: Condensed Matter,* 657**,** 414812.
7. EL-MALLAWANY, R., RIBEIRO, M. A., LARA, L. S., LENZI, E. K., ALSADIG, I. A. A. & NOVATSKI, A. 2021. Refractive index behavior of tellurite glasses. *Optical Materials,* 112**,** 110810.
8. EL GHANDOOR, H., ZIDAN, H. M., KHALIL, M. M. H. & ISMAIL, M. I. M. 2012. Synthesis and Some Physical Properties of Magnetite (Fe3O4) Nanoparticles. *International Journal of Electrochemical Science,* 7**,** 5734-5745.
9. ELKHOSHKHANY, N., EL-MALLAWANY, R. & SYALA, E. 2016. Mechanical and thermal properties of TeO2–Bi2O3–V2O5–Na2O–TiO2 glass system. *Ceramics International,* 42**,** 19218-19224.
10. ELKHOSHKHANY, N. & SYALA, E. 2017. Kinetic characterization of TeO2–Bi2O3 –V2O5 –Na2O –TiO2 glass system. *Ceramics International,* 43**,** 6156-6162.
11. ELLIOTT, S. R. 1994. Frequency-dependent conductivity in ionically and electronically conducting amorphous solids. *Solid State Ionics***,** 27-40.
12. FONG, W. L., BASHAR, K. A., BAKI, S. O., ZAID, M. H. M., GOH, B. T. & MAHDI, M. A. 2021. Thermal, structural and optical properties of Bi2O3-Na2O-TiO2-ZnO-TeO2 glass system. *Journal of Non-Crystalline Solids,* 555**,** 120621.
13. HATHOT, S. F., JUBIER, N. J., HASSANI, R. H. & SALIM, A. A. 2021. Physical and elastic properties of TeO2-Gd2O3 glasses: Role of zinc oxide contents variation. *Optik,* 247**,** 167941.
14. KABALCI, I., ZHENG, J., WANG, L., TAN, L., XUE, Y., ZHANG, Z. & PENG, M. 2017. Novel compositions of Bi2O3-ZnO-TeO2 glasses: Structure and hardness analysis. *Journal of Non-Crystalline Solids,* 464**,** 23-29.
15. LUCACEL, R. C., MARCUS, I. C., ARDELEAN, I. & HULPUS, O. 2010. Structural studies of copper doped 2TeO2–PbO–Ag2O glass by FT-IR and Raman spectroscopies. *Eur. Phys. J. Appl. Phys.,* 51**,** 30901.
16. MANDAL, A., MODAK, N., PATRA, D., MONDAL, R., DAS, A. S., KABI, S., CHAKRABARTI, C. & BISWAS, D. 2023. Effect of incorporation of alkali earth metal oxide on structural, optical and DC conduction mechanism in tellurium-phosphate glassy systems. *Journal of Materials Science: Materials in Electronics,* 34**,** 528.
17. MONDAL, R., BISWAS, D., DAS, A. S., NINGTHEMCHA, R. K. N., DEB, D., BHATTACHARYA, S. & KABI, S. 2020. Influence of samarium content on structural, thermal, linear and non-linear optical properties of ZnO–TeO2–P2O5 glasses. *Materials Chemistry and Physics,* 255**,** 123561.
18. MONDAL, R., MONDAL, S., TUDU, P., CHATTERJEE, P., KABI, S., DAS, A. S., CHATTOPADHYAY, S. & BISWAS, D. 2023. Tunable band gap, CB and VB positions of multicomponent Se65-xTe20Ge15Snx chalcogenide glassy systems: Effect of metallic additives on physical and optical parameters. *Materials Chemistry and Physics,* 296**,** 127187.
19. MURUGAN, G. S., FARGIN, E., RODRIGUEZ, V., ADAMIETZ, F., COUZI, M., BUFFETEAU, T. & COUSTUMER, P. L. 2004. Temperature-assisted electrical poling of TeO2–Bi2O3–ZnO glasses for non-linear optical applications. *Journal of Non-Crystalline Solids,* 344**,** 158-166.
20. NARASIMHA RAO, N., KITYK, I. V., RAVI KUMAR, V., RAGHAVA RAO, P., RAGHAVAIAH, B. V., CZAJA, P., RAKUS, P. & VEERAIAH, N. 2012. Piezoelectric and elastic properties of ZnF2–PbO–TeO2: TiO2 glass ceramics. *Journal of Non-Crystalline Solids,* 358**,** 702-710.
21. OSIPOV, A. A., LIŠKA, M., OSIPOVA, L. M., CHROMČIKOVÁ, M. & HRUŠKA, B. 2020. Thermodynamic modeling and Raman spectroscopy study of Na2O-TiO2-SiO2 glasses. *Vibrational Spectroscopy,* 111**,** 103160.
22. RAO, K. J., RAO, B. G. & ELLIOTT, S. R. 1985. Glass formation in the system PbO-PbCl2. *Journal of Materials Science,* 20**,** 1678-1682.
23. SADDEEK, Y., ISSA, S., ALHARBI, T., ALY, K., AHMAD, M. & TEKIN, H. O. 2019. Mechanical and nuclear shielding properties of sodium cadmium borate glasses: Impact of cadmium oxide additive. *Ceramics International,* 46.
24. SADDEEK, Y. B., YAHIA, I. S., ALY, K. A. & DOBROWOLSKI, W. 2010. Spectroscopic, mechanical and magnetic characterization of some bismuth borate glasses containing gadolinium ions. *Solid State Sciences,* 12**,** 1426-1434.

25. SHAABAN, K. S. & YOUSEF, E. S. 2020. Optical properties of Bi2O3 doped boro tellurite glasses and glass ceramics. *Optik,* 203**,** 163976.
26. SIDEK, H. A. A., ROSMAWATI, S., TALIB, Z. A., HALIMAH, M. K. & DAUD, W. M. 2009. Synthesis and Optical Properties of ZnO-TeO2 Glass System. *American Journal of Applied Sciences,* 6.
27. SINGH, Y. B., BISWAS, D., SHAH, S. K., SHAW, S., MONDAL, R., DAS, A. S., KABI, S. & SINGH, L. S. 2021a. Investigation of optical properties and electrical conductivity mechanism of Fe2O3–Sm2O3–ZnO–P2O5 quaternary glass nanocomposite systems. *Materialia,* 15**,** 100963.
28. URBACH, F. 1953. The Long-Wavelength Edge of Photographic Sensitivity and of the Electronic Absorption of Solids. *Physical Review,* 92**,** 1324-1324.
29. YADAV, A., KUMAR, A., SHARMA, K. & SHUKLA, M. K. 2019. Investigating the Effects of Amine Functionalized Graphene on the Mechanical Properties of Epoxy Nanocomposites. *Materials Today: Proceedings,* 11**,** 837-842.
30. ZHANG, S., ZHANG, Y., GAO, J., QU, Z. & ZHANG, Z. 2019. Effects of Cr2O3 and CaF2 on the structure, crystal growth behavior, and properties of augite-based glass ceramics. *Journal of the European Ceramic Society,* 39**,** 4283-4291.

